Elaboration of Fe3O4/ZnO nanocomposite with highly performance photocatalytic activity for degradation methylene blue under visible light irradiation

Rania Elshypany, Hanaa Selim, K. Zakaria, Ahmed H. Moustafa, Sadeek A.Sadeek, S.I. Sharaa, Patrice Raynaud, Amr A. Nada

Elaboration of Fe_3O_4/ZnO nanocomposite with highly performance photocatalytic activity for degradation methylene blue under visible light irradiation

Rania elshypany[a], Hanaa Selim[a], k. Zakaria[a], Ahmed H. Moustafa[b], Sadeek. A. Sadeek[b], S.I.shara[a], Patrice Raynaud[c], Amr A. Nada[a,*]

[a] Department of Analysis and Evaluation, Egyptian Petroleum Research Institute, Nasr City, Cairo, 11727, Egypt

[b] Department of Chemistry, Faculty of Science, Zagazig University, Zagazig, 44519 Egypt.

[c] Laboratoire Plasma et Conversion d'Energie (LAPLACE), Université de Toulouse, CNRS, INPT, UPS, 31062, Toulouse, France.

* (A.A. NADA) amr.nada@epri.sci.eg, chem_amr@yahoo.com

ABSTRACT

The magnetite/zinc oxide (Fe_3O_4/ZnO) nanocomposites were synthesised by the solid-state method using different ratios of zinc oxide and iron oxide. The structural, morphological, and optical properties of nanocomposites were analysed by X-ray diffraction (XRD), Fourier transform infrared spectra (FT-IR), Raman spectroscopy, transmission electron microscope (TEM), UV−Vis diffuse reflectance spectra (UV-Vis/DRS) and Photoluminescence (PL) spectrophotometry. A significant Raman shift which recorded in nanocomposite due to the ZnO component which is strongly incorporated with the magnetic Fe_3O_4 nanoparticles. Furthermore, Fe_3O_4/ZnO has a strongly quenching in PL intensity indicating stability between electrons and holes (e^-/h^+). The photocatalytic activities of Fe_3O_4/ZnO nanocomposites were investigated by the degradation of methylene blue in aqueous solution under visible light in different condition of pH, initial concentration and different trapping agents for free radicals (Tert-butyl alcohol (TBA), p-benzoquinone (BQ) and disodium ethylenediaminetetraacetic acid (Na_2-EDTA)). The results revealed that the photodegradation efficiency of ZnO compound with presence of magnetite improved from 13.5% to 88.5%. The optical results show enhancement of nanocomposite absorption under the visible region with a high life time between e^-/h^+ at the optimum ratio between Fe_3O_4/ZnO (MZ4), which can applied to obtain high photocatalytic degradation of methylene blue under visible light. Finally, the catalytic activity has been stabled when such photocatalyst was utilized again for several cycles.

Keywords: Magnetite, zinc oxide, water remediation, photocatalysis and Photo-degradation.

Highlight:

- Magnetic zinc oxide was elaborated through facile and rapid solid-state method.
- Fe_3O_4/ZnO has superior photocatalytic activity under visible light.
- The photocatalytic efficiency improved to 88.5% for MB degradation.
- Fe_3O_4/ZnO has high activity to water remediation without secondary pollution.
- The photocatalytic mechanism is based on the synergistic effect of Fe_3O_4 and ZnO.

1. Introduction

In recent decades, water contamination has become one of the dominant problems [1-3]. One of the harmful compounds in water is methylene blue (MB) [4-6]. MB is a cationic dye used in different applications as the wood and textile industries [4, 5]. In industry, the remediation of water from MB is a major problem, as failure to removal it has led to hazards in living organisms and the environment. Recently, various techniques for MB removal in aqueous media have been developed such as adsorption [6, 7], biosorption mechanism [4], membrane [8], Fenton [9] and photocatalytic process [10]. Most of the normal techniques for MB removal have limitations, as they result in secondary pollutants like adsorption and biosorption mechanism, or they are expensive such as the membrane process [10]. However, the photocatalytic technique for the degradation of hazardous substance becomes significant [11-13], due to its unique advantages without producing secondary pollutants. The photocatalyst degrades the harmful substance into friendly components as carbon dioxide and water [14, 15]. Specially, when the photocatalyst has magnetic properties, it is easy to be utilized for several times.

Over the past years, researchers in the major of water treatment have focused on the improvement of nano materials which act as photocatalysts [16-27]. Several semiconductors such as SnO_2, WO_3,TiO_2, CeO_2, and ZnO have been utilized as heterogeneous photocatalysis [28, 29]. Most of these semiconductors have a wide-band-gap, which requires ultraviolet light to be active [30, 31]. Among these semiconductors, ZnO is one of the excellent photocatalytic material because of its high catalytic activity and being environmentally friendly [32, 33]. ZnO nanoparticles has a huge surface area and a large number of active sites [34]. ZnO is classified as an n-type semiconductor [35]. It has a wide band gap energy of approximately 3.37 eV [35]. The large band gap of ZnO leaded to its excitations in the UV range below 400 nm. The high level of electrons/holes recombination is another restriction associated with ZnO [36, 37]. This deficit can be remediated by modifying ZnO [34]. This modification enhanced the absorption to be in the

visible light irradiation. Moreover, it reduces the rate of recombination between electrons/holes. Therefore, various systems have been implemented to overcome the drawbacks of ZnO, for example, doping, modification of the surface with metal nanoparticles, and the advancement of heterostructure [34, 38, 39]. Among these, the coupling ZnO with p type materials as Fe_3O_4 can increase the range of light absorption and accelerate the separation rate of the electron-hole pairs [40]. Thus, the photocatalytic performance of the Fe_3O_4/ZnO nanocomposite is assumed to be more active due to the electrons/holes separation in the p-n junction [41]. Moreover, the current magnetic properties make photocatalysts more easy to isolate and reuse from wastewater following the utilization of an external magnet [1, 42-44].

There are some scientists interested in fabricating Fe_3O_4/ZnO in order to enhance its photocatalytic activity through different preparation methods to obtain different structure and morphology. C. Karunakaran and co-workers [45] reported that the core-shell of Fe_3O_4/ZnO nanosheets by hydrothermal synthesis allows the band gap of Fe_3O_4 to be conjugated inside the band gap of ZnO for 98.5 %, 25% photodegradation of 25 ppm methylene blue under UV and visible light, respectively. The core-shell structure has a limited activity under visible light than UV source. Also, the core-shell structure of Fe_3O_4/ZnO was studied by M. Nikazar et al. [46] for phenol photodegradation to obtain a removal rate of 88% under UV irradiation. However, the same structure of core-shell was synthesized by Q. Feng et al. [47], then enhance it by graphene oxide to be active under visible illumination for the degradation of methyl orange. Furthermore, O. Długosz et al. [48] evaporated Fe_3O_4/ZnO by microwave process to recorded 63% removal percent of methylene blue. We can conclude that from previous studies the photocatalytic activity of Fe_3O_4/ZnO depend on the preparation method and the structure of the nanocomposite.

In this study, we demonstrate that Fe_3O_4/ZnO by the solid-state method is a rapid and easy method with changing the ratio between Fe_3O_4 and ZnO to get the optimum ratio between them. Among all techniques utilized to synthesize magnetite / zinc oxide, solid state is a cost-effective and simple technique. The crystalline structure, chemical states and morphology of the prepared photocatalyst were characterized by XRD, Raman, FTIR, XPS and TEM techniques. Furthermore, the optical properties were investigated by photoluminescence and UV-Vis spectroscopies. Finally, the photocatalytic activity of Fe_3O_4/ZnO nanocomposite was detected by degradation of methylene-blue (MB) under visible light illumination and with different conditions as an applied

trapping agent. Moreover, the prepared photocatalyst has high efficiency for easy extraction and reuse again.

2. Experimental

2.1. Materials

Zinc nitrate hexahydrate ($Zn(NO_3)_2.6H_2O$) (98%, CAS Number: 10196-18-6), ferrous sulphate heptahydrate ($FeSO_4.7H_2O$) with purity (99.5%, CAS Number: 7782-63-0), iron chloride hexahydrate ($FeCl_3.6H_2O$) (97%, CAS Number: 10025-77-1), methylene blue (MB) (CAS Number: 122965-43-9) and sodium hydroxide (NaOH) (98%, CAS Number: 1310-73-2) were obtained from Sigma-Aldrich organization. Ethanol was purchased from Honeywell organization with high immaculateness of 99.8 %. All purchased compounds were used as received, with no further purification.

2.2. Nanoparticle synthesis

2.2.1. Synthesis of ZnO nanoparticles (Z)

ZnO nanoparticles (ZnO NPs) were synthesized by precipitation method [49]. 6mM of Zn $(NO_3)_2.6H_2O$ was dissolved in 25 mL distilled water with stirring for 30 minutes at 100 ^oC. The pH value was adjusted at 12 by using 1M NaOH and stirring it for 1 h. The white precipitate was collected by centrifugation at a speed of 4000 rpm. The obtained precipitate was washed several times with deionized water and ethanol, then dried at 60 ^oC for 6 hrs in an electric oven and calcined at 600^oC for 2hrs in air.

2.2.2. Synthesis of Fe_3O_4 magnetics nanoparticles (M)

Fe_3O_4 magnetic nanoparticles (Fe_3O_4 NPs) were prepared via co-precipitation method. We used ferrous and ferric salts in a ratio of 1:2 M ratio in the presence of N_2 gas as recorded in our previous study [42]. The relevant chemical reaction can be expressed as follows:

$$Fe^{2+} + 2Fe^{3+} + 8OH^- \rightarrow Fe_3O_4 + 4H_2O \qquad \text{(eq.1)}$$

2.2.3. Synthesis of Fe_3O_4/ZnO nanocomposites (MZ) by solid state method

MZ was prepared by thermolysis process and calcination at 600 ^oC for 4 h by solid state method [18, 23, 50]. With different weight ratios of M:Z (0.2:1, 0.4:1, 0.6: 1, 0.8:1 and 1:1 wt.%) and donated as MZ1, MZ2, MZ3, MZ4, and MZ5, respectively.

2.3. Characterization

The phase of the prepared samples was examined by X-ray diffraction (XRD) using a diffractometer (Panalytical XPERT PRO MPD). CuKα radiation (λ=1.5418 Å) was used at 40 kV

and 40 mA. The morphology was investigated by transmission electron microscope (TEM) model JEM-2100, JEOL, Japan. The structural study of the prepared samples was investigated by Raman spectroscopy with a 532 nm laser source and a power of 10 mW (model Sentera, Bruker, Germany). The functional groups were identified by a Fourier transform infrared spectrometer (FT-IR) model spectrum one (Perkin Elmer, USA) in the wave number range of 400 - 4000 cm^{-1}. The optical reflectance was recorded by a UV-Vis spectrometer (Perkin Elmer Lambda 1050). Photoluminescence spectra were recorded by a Cary Eclipse Fluorescence Spectrophotometer.

2.4 Photocatalytic activity study

The photocatalytic activity of MZ1, MZ2, MZ3, MZ4, and MZ5 nanocomposites was studied through the degradation of methylene blue (MB). MB was used as an organic pollutants reference in aqueous solution. The photocatalytic activity was detected under visible illumination of a halogen lamp (500 W/cm^2) placed 10 cm above the 4 cm diameter reactor tube. First, 0.2 g of prepared samples were suspended in 50 mL of aqueous methylene blue solution at a concentration of 100 ppm. The mixture was stirred for 30 min in a dark box, until adsorption-desorption equilibrium was obtained between MB dye and nanocomposite (photocatalyst) before light irradiation. Then, 3mL of the suspensions were withdrawn regularly from reactor and centrifuged to remove the catalyst. The clean centrifuged solutions were analysed by UV-vis spectrophotometer [42].

3 Results and discussion

Magnetite and zinc oxide were elaborated with different ratios to form a homogeneous nanocomposite. X-ray diffraction (XRD) was used for detecting the crystalline phase of M, Z, MZ1, MZ2, MZ3, MZ4 and MZ5 as presented in Figure 1, which demonstrates two sets of diffraction peaks. The first set for ZnO is well indexed to hexagonal wurtzite structure (JCPDS Card No. 01-080-4199) with the planes (100), (002), (101), (102), (110), (103), (200), (112) and (201) corresponding to 2Θ = 31.7, 34.4, 36.2, 47.5, 56.5, 62.8, 66.3, 67.9 and 69.0^o, respectively [51]. (Give here the signification of 2Θ). The preferred growth orientation is along the (101) crystallographic direction. The strong sharp peaks suggested that the ZnO NPs were prepared in high crystalline [52]. The other set of magnetite Fe_3O_4 phase (JCPDS Card no. 01- 089-1397) with diffraction peaks at 30.00, 35.50, 43.14, 53.44, 57.40, and 62.58^o corresponding to Miller indices (220), (311), (400), (422), (511), and (440), respectively [53]. These peaks are attributed to the cubic spinal structured magnetite. No significant peaks corresponding to impurities were detected

in the XRD pattern. After mixing Fe_3O_4 NPs with ZnO, peaks of both magnetite and zinc oxide are detected. In the nanocomposite, some intensities of the peaks changed due to peak interference.

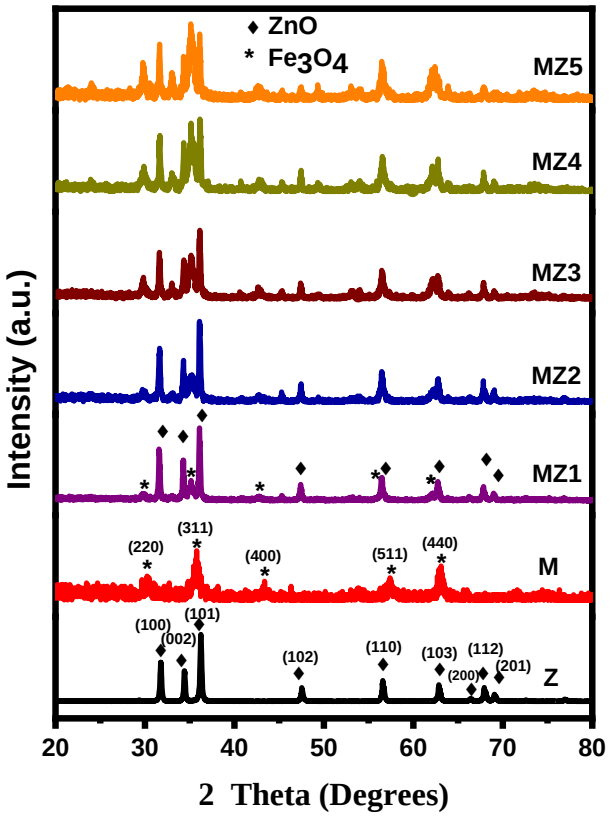

Figure 1. XRD spectra of Z, M, MZ1, MZ2, MZ3, MZ4 and MZ5 nanocomposites.

The Raman spectra of all prepared samples are shown in Figure 2. The normal vibrational modes of ZnO have $A_1+2E_2+2B_1+E_1$ [54], where A_1 and E_1 consist of two modes: Longitudinal Optical (LO) and Transverse Optical (TO). B_1 is inactive Raman. E_2 consists of two modes: high frequency phonon E_{2H} and low frequency phonon E_{2L} [55]. The peak at 435.5 cm^{-1} in the Raman spectrum of Z sample is assigned to E_{2H} mode of ZnO (the strongest mode). The peak at 328 cm^{-1} assigned to A_{1T}. And the peak at 576 cm^{-1} is assigned to A_{1L} (longitudinal optical (LO) mode). Nonetheless the A_{1L} phonon peak of bulk ZnO showed reached 574 cm^{-1} [56]. In contrast, the M sample (Fe_3O_4) has peaks at 218.5, 282, 396 and 652.5 cm^{-1} and they correspond to A_{1g}, E_g, E_g and A_{1g}, respectively [50, 57, 58]. Compared with pure ZnO nanocrystals, the A_{1L} mode of the Fe_3O_4/ZnO nanocomposites appeared in the blue shift at peak 609.9 cm^{-1}. When the

electromagnetic radiation transmits through the Fe_3O_4/ZnO nanocomposites, the polarization of the ZnO component will be strongly influenced by the incorporation with Fe_3O_4 magnetic nanoparticles. Hence the excited electrode dipoles result in a vibrational frequency shift. Furthermore, the contributing factor could be the interfacial charge shift between Fe_3O_4 and ZnO, which was replaced by electrons in the nanocomposite materials were catalysed from the ZnO nanocrystals, then they will expend and absorb into the Fe_3O_4 nanoparticles. This is followed by recombination with the remaining holes at the ZnO-Fe_3O_4 interface leading to a frequency shift [59]. Moreover, the relative intensity of A1T and A1L (ZnO) during the limitation of the ZnO quantity in nanocomposites decreased gradually from MZ1 to MZ5. In addition, the peak cat 1310 cm^{-1} related to the scattering of two magnon were observed in the nanocomposites due to the presence of scattering generated from the antiparallel spin of two magnons, where the homogeneity and synergism between ZnO and Fe_3O_4 were confirmed [50]. Figure S1 demonstrates the FT-IR spectra of ZnO, Fe_3O_4 and Fe_3O_4/ZnO nanocomposite before the degradation of MB, which was performed in the range of 400 - 4,000 cm^{-1}. The characteristic bond of ZnO is well observed at 449 cm^{-1}. The weak band near 1637.8 cm^{-1} is attributed to the H-O-H bending vibration due to adsorbed water on the surface of nanoparticles. The broad peak centred around 3400 cm^{-1} corresponds to the stretching vibration mode of hydroxyl groups ($^{-}$OH) [60]. Also, the band at 568 cm^{-1} is assigned to Fe-O bond vibration mode [61, 62]. The FT-IR spectra of Fe_3O_4/ZnO nanocomposite were identical to the hybridization of ZnO nanocrystals with Fe_3O_4 [63], taking into consideration that coupling Fe_3O_4 with ZnO should to be homogeneous.

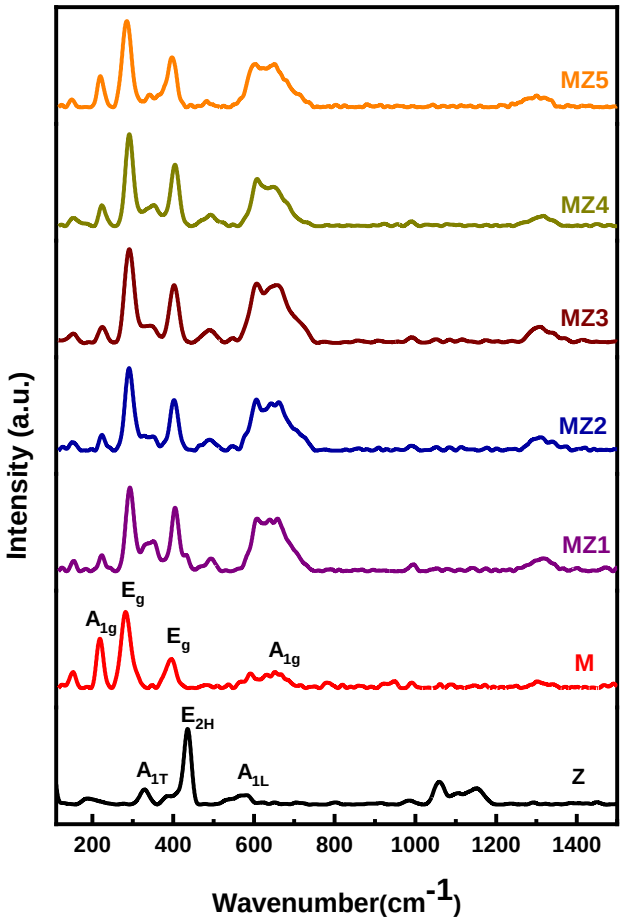

Figure 2. Raman spectra of the Z, M, MZ1, MZ2, MZ3, MZ4 and MZ5 nanocomposites.

Furthermore, the chemical composition of Fe_3O_4/ZnO (MZ4) was detected by X-ray photoelectron spectroscopy analysis (XPS) as presented in Figure 3a-c. The XPS spectra of iron have two peaks of Fe_3O_4: 2p3/2 and 2p1/2 at 711.5 and 723.7 eV, respectively [50, 64] (in Figure 3-a) which are matched with XRD and Raman. In addition, the zinc peak at 121 eV corresponds to Zn 2p3/2 which it was bound to ZnO in Figure 3-b [65]. XPS of oxygen 1s in Figure 3-c at 530.4 eV related to lattice oxygen (O_L) [66] in the Fe_3O_4/ZnO nanocomposite.

Moreover, the morphology of prepared nanocomposites was detected by transmission electron microscopy. TEM images of the Z, M, MZ1, MZ4, and MZ5 nanocomposites are presented in Figure 4a-e. The presence of homogeneous nanocrystalline ZnO particles with spherical shapes and weak agglomeration is observed in Figure 4a) [50]. Figure 4b shows the iron

oxide nanoparticles exhibiting a cubic morphology [50, 67] and Figures 4c-e for Fe_3O_4/ZnO composites show the cubic and spherical morphology with average diameter 15 ± 2 nm and 20 ± 4 nm for Fe_3O_4 and ZnO, respectively as the nanocomposites structure. In addition, the MZ4 nanocomposite has a uniform distribution without accumulation. In addition, the elemental composition of the nanocomposites by EDX presented in Table S1 which confirmed the atomic ratio between Fe_3O_4 and ZnO which is in consistent with the experimental values.

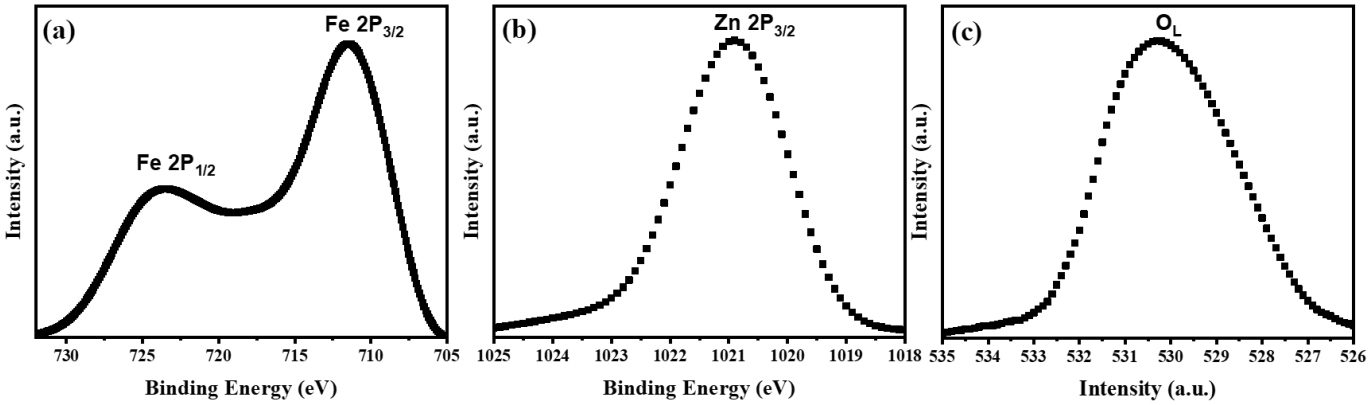

Figure 3. XPS spectra of MZ4 (a) Fe 2P; (b) Zn 2P and (c) O 1S

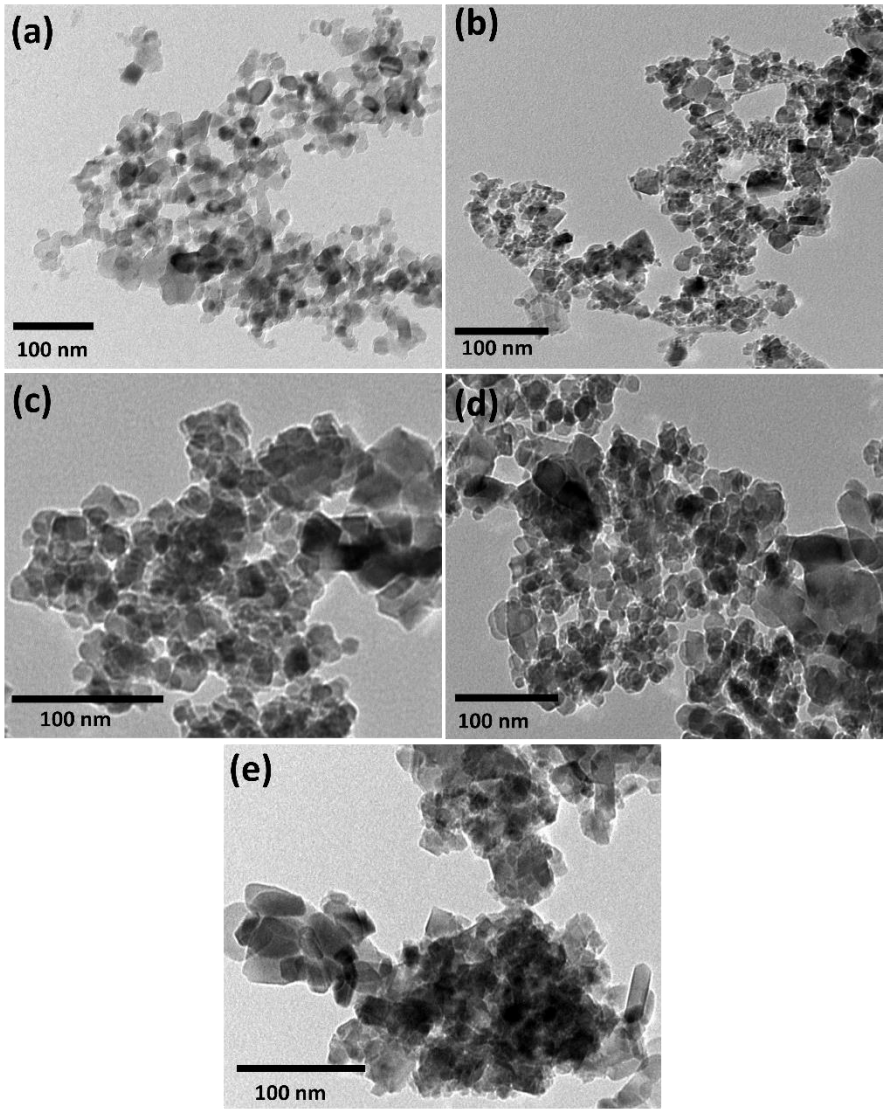

Figure 4. TEM images of (a)ZnO Nps, (b) Fe_3O_4, (c) MZ1, (d) MZ4 and (e) MZ5

3.2 Optical analysis

There are several mechanisms that control photocatalytic activity: the production of electron / hole pairs, photoabsorption, charge / carrier transfer, and charge carrier utilization. The optimization of the photocatalytic activity depends on the efficiency of the product and the transfer of the e^- / h^+ pairs, which depends on the energy band gap (Eg) of the photocatalyst. The energy band gap values (Eg) of the samples were determined according to the following equations [31, 32]: $\alpha hv = A(hv - Eg)^{n/2}$ (eq.2)

Where α is the absorption coefficient, ν is the frequency of light and n is the constant of proportionality. The n value is determined by the transition of the semiconductor, i.e., the direct transition as in the prepared nanocomposite (n = 1). The DRS spectra of the prepared ZnO, Fe_3O_4, MZ1, MZ2, MZ3, MZ4 and MZ5 NPs are shown in figure 5. The band gap value of pure ZnO NP is 3.20 eV. However, the band gap of the Fe_3O_4/ZnO nanocomposites shifted towards the redshift in the presence of magnetite and there are two bandgaps for all samples according to Table 1. The conjugation of two bands gap led to more stability between the e^-/h^+ pairs. Moreover, Fe_3O_4/ZnO nanocomposites can be excited under visible light to give more electron-hole pairs.

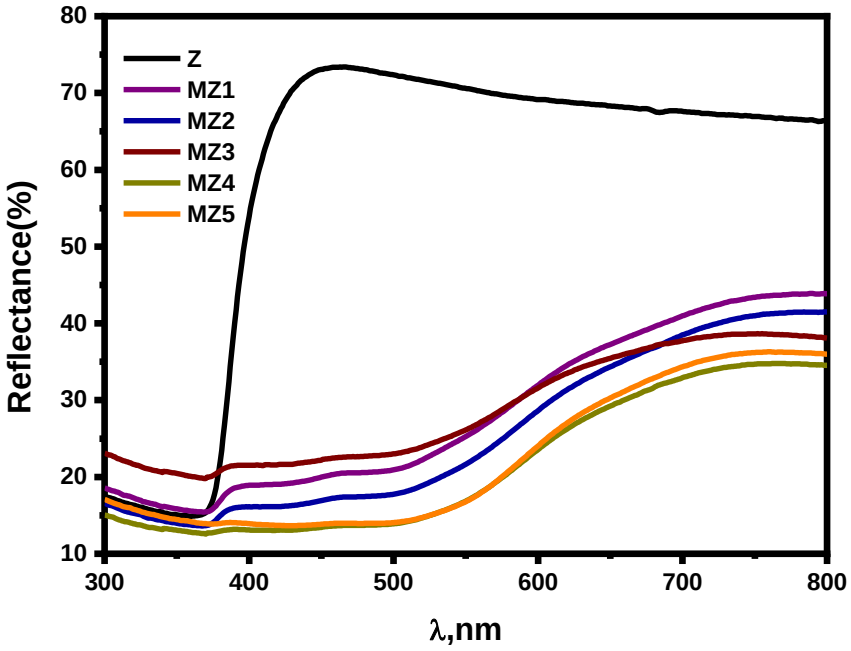

Figure 5. UV–Vis diffuse reflectance spectra of Z, MZ1, MZ2, MZ3, MZ4 and MZ5 nanocomposites.

Table 1. The band gap and kinetic parameters for photocatalytic activities of ZnO, MZ1, MZ2, MZ3, MZ4, and MZ5 NPs.

Sample name	E_g (eV)(Fe_3O_4)	E_g(eV)(ZnO)	K_a (min^{-1})	A_{OC} ($TW.h/m^3$)
MB	--	--	2.468E-4 ± 6E-5	563.1
ZnO	--	3.20	9.217E-4 ± 9.582E-5	150.8

MZ1	2.12	3.19	0.009 ± 8.373E-4	15.4
MZ2	2.11	3.19	0.011 ± 5.776E-4	12.6
MZ3	2.09	3.12	0.014 ± 9.106E-4	9.9
MZ4	2.07	3.09	0.018 ± 0.001	7.7
MZ5	2.08	3.06	0.009 ± 6.141E-4	15.4

The room temperature photoluminescence (PL) spectra of all prepared samples were shown in Figure 6. PL spectrum of pure ZnO shows a strong emission band at 381 nm. In addition, some peaks at 406 nm, 420 nm and 445 nm appear due to deep level emission (DLE) [68]. A strong quenching of PL intensity after incorporation of Fe_3O_4 with ZnO, indicating that the recombination between photo-electrons generated and holes is reduced.

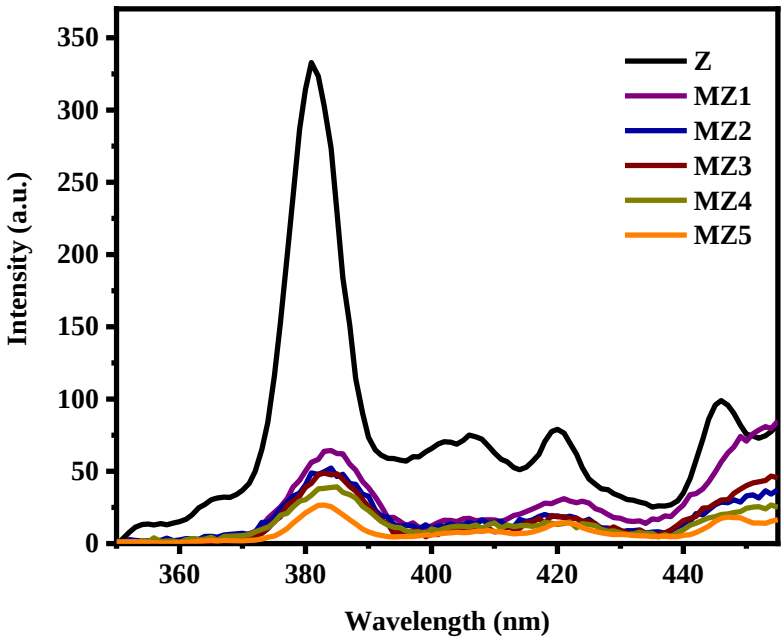

Figure 6. Photoluminescence spectra of Z, MZ1, MZ2, MZ3, MZ4 and MZ5 nanocomposites.

3.3. Photocatalytic activity

The photocatalytic efficiency of the (MZ1, MZ2, MZ3, MZ4 and MZ5) nanocomposites was evaluated for MB under visible light irradiation (wavelength > 400 nm). MB was chosen as an organic pollutant model. Figure 7.a shows the degradation of MB concentration for all the

prepared nanocomposites. The MZ4 NCs shows the strongest degradation of MB, implying the highest photocatalytic activity, followed by MZ3, MZ2, MZ5 and MZ1. Figure 7.b, shows the degradation of kinetic linear curves, where the photodegradation reactions follow a Langmuir-Hinshelwood first-order kinetics model as shown in the following equation:

$R = dC / dt = kKC / (1+KC)$ (eq.3)

Where r is the degradation rate of MB (mg L^{-1} min^{-1}), C is the concentration of the MB solution (mg L^{-1}), t is the irradiation time, k is the reaction rate constant (mg L^{-1} min^{-1}), and K is the adsorption coefficient of MB (mg L^{-1}). The relationship between ln (C_0/C) and the reaction time (t) showed that the decomposition of MB with different photocatalysts follows a pseudo-first-order kinetic

$\ln (C_0/C) = k\,KT = k_a\,t$ (eq.4)

Where k_a is the apparent first-order rate constant (min^{-1}), C_o is the concentration at time =0 of irradiation, and C is the concentration at time t.

k_a values obtained from the linear relation between ln (C_0/C) and time are reported in Table 1 and increased in the following order: MZ4>MZ3>MZ2>MZ5>MZ1>ZnO>MB meaning MZ4 sample shows the best activity. In addition, MZ4 has a higher photocatalytic efficiency under visible light irradiation compared to previous studies Table 2. Beside the kinetic study, an important factor for judging materials is Figure of Merit (FOM). FOM in our case is based on international union of pure and applied chemistry (IUPAC) for photocatalytic process defined as collector area per order (A_{CO}) due to the reaction process follow first order kinetics [69, 70]. The Figure of Merit (FOM) for all the prepared nanocomposite illustrated in Table 1, where A_{CO} was defined by the following equation:

$$A_{co} = \frac{A\bar{E}_s t}{V\,log(C_i/C_F)} \quad \text{(eq.5)}$$

Where, A (m^2) is the light-exposed area, $\bar{E}_s$ is the average solar irradiance (W/m^2), t is time of illumination (h), V is volume of reactor (m^3), C_i and C_f are the initial and final concertation of pollutant. Furthermore, the equation supposes first order kinetics, so log (C_i/C_f) = 0.434 k_a t; where: t is time (h) and k_a is the apparent first-order rate constant (h^{-1}) [69, 70]. Equation 4 will be as following:

$$A_{co} = \frac{A\bar{E}_s}{0.434\,VK_a} \quad \text{(eq.6)}$$

In addition, the pH-changing during the photodegradation was detected on order to obtain more information about MB photodegradation under different condition for MZ4 as presented in Figure 7.c. The results indicated that the pH of the solution has a changing effect of the MB photodegradation process by MZ4 due to the electrostatic interactions between the substrate, the photocatalyst and the charged produced radicals during the photodegradation process. Therefore, it has been very difficult to illustrate the pH effects of the MB photodegradation. The MB showed in cationic form at pH=5 and MZ4 has negatively charged. Therefore, there is electrostatic attraction between cationic dye and MZ4. However, the best MB photodegradation recorded at pH=6 due to the presence of ideal electrostatic attraction and the ability to the free radical formation on the surface of photocatalyst. Moreover, zinc oxide was the important photocatalyst in MZ4 at that pH [71]. In addition, the pH effect on (100 ppm) MB degradation in the presence and absence of MZ4 after 2 h of visible light illumination is displayed in Figure S2. Where, MB is bleached under acidic medium without catalysts, but with a low effect not more than 10% when compared with presence of MZ4 at 88.5% removal efficiency. Furthermore, the effect of MB initial concentration was studied on its photodegradation from 50 to 200 ppm as presented in Figure 7.c. The degradation efficiency decreased with increased the initial concentration of MB due to the limitation of illumination by agglomerated MB on the photocatalyst [10, 72].

To determine the stability of (MZ4) Fe_3O_4/ZnO nanocomposite photocatalyst, recycling tests for the degradation of MB under visible light were performed on the photocatalyst, which are presented in Figure 7.d. The photocatalyst was collected by magnet then it was washed with distilled water and ethanol. IR characteristics were examined before and after photocatalytic degradation in Figure S3. Where, the same function groups have been observed in the catalyst before and after photocatalytic degradation. Thus, the prepared nanocomposite has high recovery and reusability for photocatalytic activity, in addition to studying the roles of free radical. we applied trapping agents of free radical: Tert-butyl alcohol (TBA), p-benzoquinone (BQ) and disodium ethylenediaminetetraacetic acid (Na_2-EDTA) to scavenge the hydroxyl radicals, superoxide radicals and holes, respectively as present in Figure 7.d [73]. The removal efficiency of MB changed dependent on the sacrificial agents, and the removal efficiency decreased to 39% in the presence of (5mM) TBA as hydroxyl radicals played an important role in the photodegradation of MB.

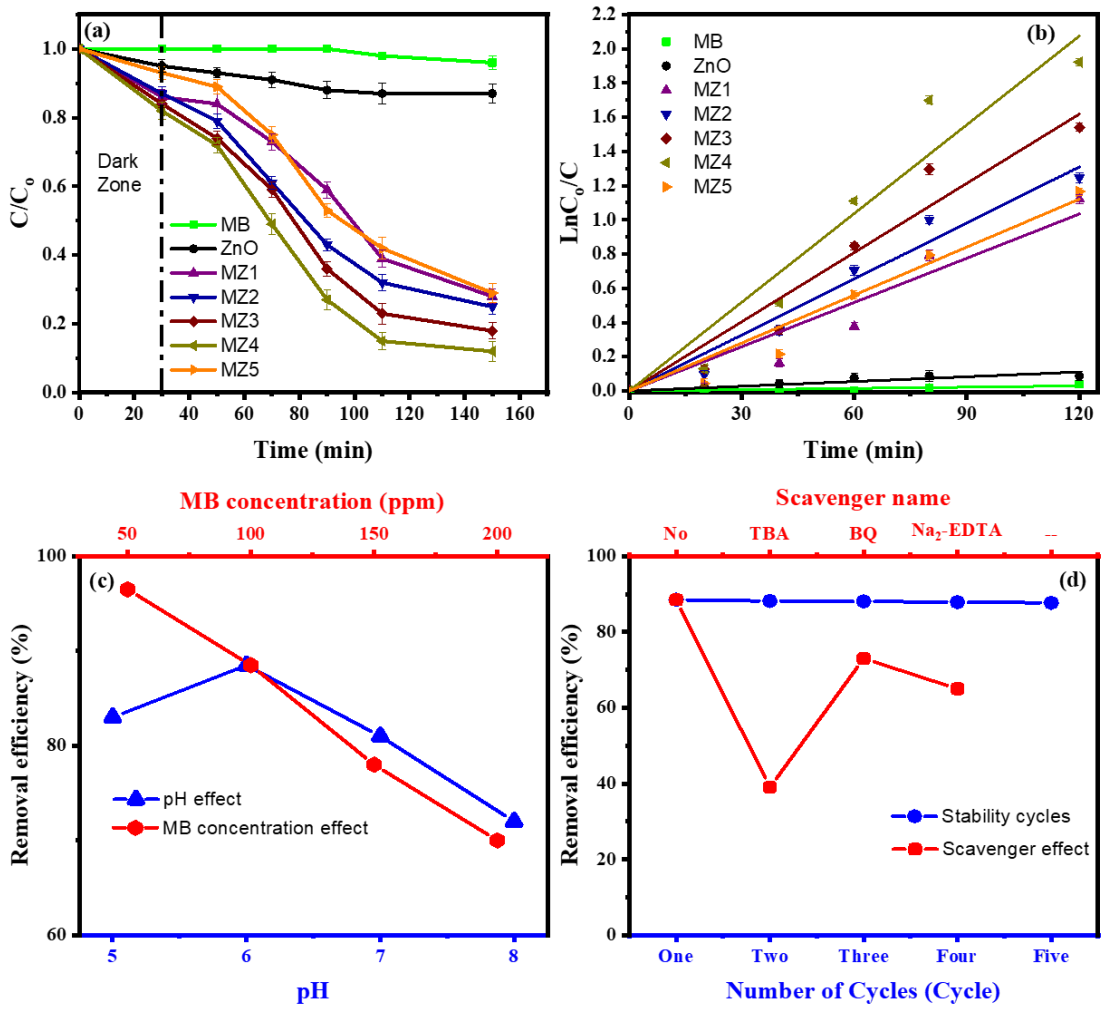

Figure 7. (a) Photodegradation and (b) Kinetic of MB by Z, MZ1, MZ2, MZ3, MZ4 and MZ5 nanocomposites for 100 ppm MB under visible light; (c) The pH and MB concentration effect for MB degradation by MZ4 after 2 h of visible light illumination; and (d) The stability cycles and scavenger study effect for MB degradation by MZ4 for 100 ppm MB after 2 h of visible-light illumination.

Table 2. Photo catalytic degradation of MB under Visible Light with Various Photocatalysts.

photocatalyst	Weight of catalyst (g/L)	Concentration of MB (ppm)	Time(h)	Degradation (%)	Ref.

$Fe_3O_4/CdWO_4 + H_2O_2$	0.1	20	2	32	[74]
Fe_3O_4 /$CdWO_4$ /$PrVO_4$ $+H_2O_2$	0.1	20	2	68	[74]
WO_3-GO	0.5	3	1.2	82	[75]
Pt/ZnO-MWCNT	0.4	100	1	74	[76]
$Zn_3(OH)_2V_2O_7 \cdot 2H_2O$	2	10	3	47.7	[77]
$Fe_3O_4/ZnWO_4/CeVO_4$ $+H_2O_2$	0.6	25	2	84	[78]
Fe_3O_4/ZnO	0.2	100	2	88.5	Our work

The degradation mechanism based on all previous results and the energy band of hereto structure of magnetite ZnO is shown in Figure 8. When ZnO and Fe_3O_4 are coupled together, photons may be absorbed in both ZnO and Fe_3O_4 and form the electron/hole pairs. Where, ZnO and Fe_3O_4 have a positions of conduction bands (-0.45 eV and -0.58 eV vs NHE) and valence bands (+ 2.75 eV and + 0.99 eV vs NHE), respectively [79, 80]. The electrons of the conduction Band (CB) of Fe_3O_4 would migrate to that of the ZnO. Whereas holes at the valence Band (VB) of Fe_3O_4 would remain there. This process reduces the probability of the electron/hole recombination. Therefore, there is an enhancement of photocatalytic activities of the Fe_3O_4/ZnO compared to the pure ZnO. After that the OH^- present in the aqueous solution is captured by the hole of the valence band to form highly reactive $OH^\cdot$ Radical. Then, the dye molecules attacked by this radical are decomposed into simple products [81, 82]. This can be described by the following steps:

1) Photoexcitation

   Photoelectron is transfered from valence band (filled) of a semiconductor to conduction band (empty).

2) Ionization of water

   Holes in the valence band react with water to produce $OH^\cdot$ radical

3) Oxygen ionosorption

   Electron in conduction band is taken by oxygen to produce superoxide radical $O_2^{\cdot -}$

$$Fe_3O_4/ZnO \longrightarrow Fe_3O_4/ZnO\ (h^+) + Fe_3O_4/ZnO\ (e^-) \qquad \text{(eq.7)}$$

$$Fe_3O_4/ZnO\ (e^-) + O_2 \longrightarrow O_2^{\cdot -} \qquad \text{(eq.8)}$$

$Fe_3O_4/ZnO\ (h^+) + H_2O \longrightarrow OH\cdot + H^+$ (eq.9)

$H_2O + O_2^{\cdot -} \longrightarrow 2\ \cdot OH$ (eq.10)

$\cdot OH + MB \longrightarrow$ degredation products (eq.11)

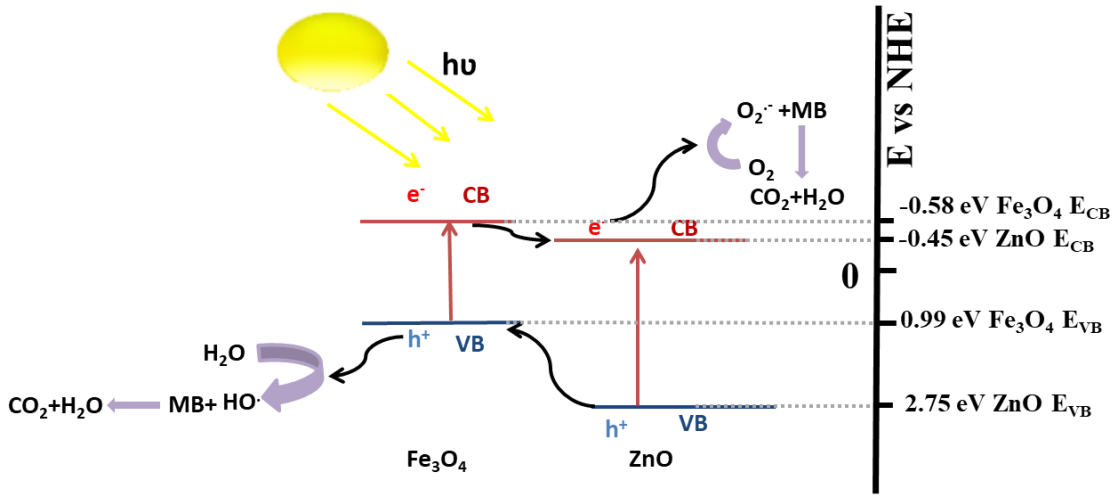

Figure 8. Schematic diagram of the MZ4 photocatalytic activity mechanism.

4. Conclusion

The Fe_3O_4/ZnO nanocomposite was successfully synthesized by a solid-state process under the optimal conditions achieved at 600 ºC for 4 h with different ratios between Fe_3O_4 and ZnO. The XRD, XPS, TEM, Raman and FT-IR spectroscopy measurement contributed to the understanding of the structural phase of Fe_3O_4/ZnO nanocomposites. All characterization techniques confirmed the strong incorporation between Fe_3O_4 and ZnO compounds, which consequently enhanced the band-gap for the nanocomposites that were recorded by UV-DRs to be active under visible light illumination. Furthermore, the heterogenous band gap between Fe_3O_4 and ZnO quenched the Photoluminescence and improved the life time of e^-/h^+. Photocatalytic activity measurements of different coupling of Fe_3O_4 with ZnO led to better activity in the degradation of MB under visible light. The highest degradation efficiency (88.5 %) was reached with sample MZ4 with high stability up to five cycles. In addition, the preferred pH for MB degradation by MZ4 under visible light is 6. The mechanism of MB degradation mainly depends on hydroxyl radical corresponding to the effect of the various trapping agents applied (TBA, BQ and Na_2-EDTA). Moreover, the prepared materials have the ability to be easily extracted from the

solution by the external magnetic field. In brief, Fe_3O_4/ZnO nanocomposites are promising photocatalysts for reducing toxic organic pollutants in wastewater.

Reference

1. El-Maghrabi, H.H., et al., *Magnetic graphene based nanocomposite for uranium scavenging.* J Hazard Mater, 2017. **322**(Pt B): p. 370-379.
2. Mohammed Ali, G.A., et al., *High Surface Area Mesoporous Silica for Hydrogen Sulfide Effective Removal.* Current Nanoscience, 2020. **16**(2): p. 226-234.
3. Najem, M., et al., *Palladium/Carbon Nanofibers by Combining Atomic Layer Deposition and Electrospinning for Organic Pollutant Degradation.* Materials (Basel), 2020. **13**(8).
4. Nas, M.S., et al., *Synthesis, characterization, kinetics and adsorption properties of Pt-Co@GO nano-adsorbent for methylene blue removal in the aquatic mediums using ultrasonic process systems.* Journal of Molecular Liquids, 2019. **296**: p. 112100.
5. Deng, H., et al., *Adsorption of methylene blue on adsorbent materials produced from cotton stalk.* Chemical Engineering Journal, 2011. **172**(1): p. 326-334.
6. Nada, A.A., et al., *Functionalization of MCM-41 with titanium oxynitride deposited via PECVD for enhanced removal of methylene blue.* Journal of Molecular Liquids, 2019. **274**: p. 505-515.
7. Medhat, A., et al., *Efficiently activated carbons from corn cob for methylene blue adsorption.* Applied Surface Science Advances, 2021. **3**: p. 100037.
8. Zhao, R., et al., *Highly flexible magnesium silicate nanofibrous membranes for effective removal of methylene blue from aqueous solution.* Chemical Engineering Journal, 2019. **359**: p. 1603-1616.
9. Liu, C., et al., *Synergetic degradation of Methylene Blue through photocatalysis and Fenton reaction on two-dimensional molybdenite-Fe.* Journal of Environmental Sciences, 2022. **111**: p. 11-23.
10. Nada, A.A., et al., *Mesoporous $ZnFe_2O_4$@TiO_2 nanofibers prepared by electrospinning coupled to PECVD as highly performing photocatalytic materials.* The Journal of Physical Chemistry C, 2017. **121**(44): p. 24669-24677.
11. Morshedy, A.S., et al., *Highly efficient Imprinted Polymer Nanocomposites for photocatalytic desulfurization of real diesel fuel.* Environmental Technology & Innovation, 2021. **21**: p. 101206.
12. Rehan, M., et al., *Development of multifunctional polyacrylonitrile/silver nanocomposite films: Antimicrobial activity, catalytic activity, electrical conductivity, UV protection and SERS-active sensor.* Journal of Materials Research and Technology, 2020. **9**(4): p. 9380-9394.
13. Tantawy, H.R., et al., *Novel synthesis of bimetallic Ag-Cu nanocatalysts for rapid oxidative and reductive degradation of anionic and cationic dyes.* Applied Surface Science Advances, 2021. **3**: p. 100056.
14. El-Maghrabi, H.H., H.R. Ali, and S.A. Younis, *Construction of a new ternary α-MoO_3–WO_3/CdS solar nanophotocatalyst towards clean water and hydrogen production from artificial wastewater using optimal design methodology.* RSC advances, 2017. **7**(8): p. 4409-4421.

15. El-Maghrabi, H.H., et al., *One pot environmental friendly nanocomposite synthesis of novel TiO_2-nanotubes on graphene sheets as effective photocatalyst.* Egyptian Journal of Petroleum, 2016. **25**(4): p. 575-584.
16. Diab, K.R., et al., *Facile fabrication of $NiTiO_3$/graphene nanocomposites for photocatalytic hydrogen generation.* Journal of Photochemistry and Photobiology A: Chemistry, 2018. **365**: p. 86-93.
17. El-Maghrabi, H.H., et al., *Coaxial nanofibers of nickel/gadolinium oxide/nickel oxide as highly effective electrocatalysts for hydrogen evolution reaction.* J Colloid Interface Sci, 2021. **587**: p. 457-466.
18. Kawrani, S., et al., *Enhancement of calcium copper titanium oxide photoelectrochemical performance using boron nitride nanosheets.* Chemical Engineering Journal, 2020. **389**: p. 124326.
19. Nada, A.A., et al., *Highly textured boron/nitrogen co-doped TiO_2 with honeycomb structure showing enhanced visible-light photoelectrocatalytic activity.* Applied Surface Science, 2020. **505**: p. 144419.
20. Nada, A.A., H. Selim, and M. Bechelany, *A novel photoelectrode of NiO@ZnO nanocomposite prepared by Pechini method coupled with PLD for efficiency enhancement in DSSCs.* Materials Science-Poland, 2018. **36**(2): p. 327-336.
21. El-Maghrabi, H.H., et al., *Photocorrosion resistant Ag_2CO_3@Fe_2O_3/TiO_2-NT nanocomposite for efficient visible light photocatalytic degradation activities.* J Hazard Mater, 2018. **360**: p. 250-256.
22. El-Maghrabi, H.H., et al., *Synthesis of mesoporous core-shell CdS@TiO_2 (0D and 1D) photocatalysts for solar-driven hydrogen fuel production.* Journal of Photochemistry and Photobiology A: Chemistry, 2018. **351**: p. 261-270.
23. Kawrani, S., et al., *Segregation of copper oxide on calcium copper titanate surface induced by Graphene Oxide for Water splitting applications.* Applied Surface Science, 2020. **516**: p. 146051.
24. Miquelot, A., et al., *In- and out-plane transport properties of chemical vapor deposited TiO_2 anatase films.* Journal of Materials Science, 2021. **56**(17): p. 10458-10476.
25. Liang, Z., et al., *Facile preparation of metallic 1T phase molybdenum selenide as cocatalyst coupled with graphitic carbon nitride for enhanced photocatalytic H_2 production.* Journal of Colloid and Interface Science, 2021. **598**: p. 172-180.
26. Qin, Y., et al., *Au nanorods decorated TiO_2 nanobelts with enhanced full solar spectrum photocatalytic antibacterial activity and the sterilization file cabinet application.* Chinese Chemical Letters, 2021. **32**(4): p. 1523-1526.
27. Sun, B., et al., *The fabrication of 1D/2D CdS nanorod@Ti_3C_2 MXene composites for good photocatalytic activity of hydrogen generation and ammonia synthesis.* Chemical Engineering Journal, 2021. **406**: p. 127177.
28. Herrmann, J.-M., *Heterogeneous photocatalysis: fundamentals and applications to the removal of various types of aqueous pollutants.* Catalysis today, 1999. **53**(1): p. 115-129.
29. Xu, L., et al., *Flower-like ZnO-Ag_2O composites: precipitation synthesis and photocatalytic activity.* Nanoscale research letters, 2013. **8**(1): p. 536.
30. Lin, C. and K.-S. Lin, *Photocatalytic oxidation of toxic organohalides with TiO2/UV: The effects of humic substances and organic mixtures.* Chemosphere, 2007. **66**(10): p. 1872-1877.

31. Abo, R., N.-A. Kummer, and B.J. Merkel, *Optimized photodegradation of Bisphenol A in water using ZnO, TiO_2 and SnO_2 photocatalysts under UV radiation as a decontamination procedure.* Drinking Water Engineering and Science, 2016. **9**(2): p. 27.
32. Yu, J. and X. Yu, *Hydrothermal synthesis and photocatalytic activity of zinc oxide hollow spheres.* Environmental science & technology, 2008. **42**(13): p. 4902-4907.
33. Hariharan, C., *Photocatalytic degradation of organic contaminants in water by ZnO nanoparticles: Revisited.* Applied Catalysis A: General, 2006. **304**: p. 55-61.
34. Li, G., et al., *High Purity Anatase TiO2 Nanocrystals: Near Room-Temperature Synthesis, Grain Growth Kinetics, and Surface Hydration Chemistry.* Journal of the American Chemical Society, 2005. **127**(24): p. 8659-8666.
35. Wang, Y., et al., *New insights into fluorinated TiO2 (brookite, anatase and rutile) nanoparticles as efficient photocatalytic redox catalysts.* RSC Advances, 2015. **5**(43): p. 34302-34313.
36. Zhou, M., J. Yu, and B. Cheng, *Effects of Fe-doping on the photocatalytic activity of mesoporous TiO2 powders prepared by an ultrasonic method.* Journal of hazardous materials, 2006. **137**(3): p. 1838-1847.
37. Estrellan, C.R., C. Salim, and H. Hinode. *Effect of Co-doping Nb with Various Transition Metals on the Photocatalytic Activity of Sol-gel Derived TiO_2*. in *Book of Abstracts of the 12th Asian Pacific Confederation of Chemical Engineering Congress (Vol 3 Materials Science and Engineering)*. 2008.
38. Thi, V.H.T. and B.-K. Lee, *Great improvement on tetracycline removal using ZnO rod-activated carbon fiber composite prepared with a facile microwave method.* Journal of hazardous materials, 2017. **324**: p. 329-339.
39. Akhundi, A. and A. Habibi-Yangjeh, *Ternary magnetic g-C3N4/Fe3O4/AgI nanocomposites: novel recyclable photocatalysts with enhanced activity in degradation of different pollutants under visible light.* Materials Chemistry and Physics, 2016. **174**: p. 59-69.
40. Cao, X., et al., *Magnetic photocatalysts with a p–n junction: Fe3O4 nanoparticle and FeWO4 nanowire heterostructures.* Nanoscale, 2014. **6**(21): p. 12366-12370.
41. El-Maghrabi, H.H., et al., *Design of Ni/NiO–TiO2/rGO nanocomposites on carbon cloth conductors via PECVD for electrocatalytic water splitting.* International Journal of Hydrogen Energy, 2020. **45**(56): p. 32000-32011.
42. Nada, A.A., et al., *Elaboration of nano titania-magnetic reduced graphene oxide for degradation of tartrazine dye in aqueous solution.* Solid State Sciences, 2018. **78**: p. 116-125.
43. Salama, K.K., et al., *A new way in synthesizing magnetic nano gel for cleaning an Egyptian Coptic fresco painting.* Mediterranean Archaeology and Archaeometry, 2017. **17**(1): p. 189-195.
44. Draz, M.A., et al., *Large scale hybrid magnetic $ZnFe_2O_4/TiO_2$ nanocomposite with highly photocatalytic activity for water splitting.* Journal of Nanoparticle Research, 2021. **23**(1).
45. Karunakaran, C., P. Vinayagamoorthy, and J. Jayabharathi, *Nonquenching of Charge Carriers by Fe3O4 Core in Fe3O4/ZnO Nanosheet Photocatalyst.* Langmuir, 2014. **30**(49): p. 15031-15039.
46. Nikazar, M., et al., *The optimum conditions for synthesis of Fe3O4/ZnO core/shell magnetic nanoparticles for photodegradation of phenol.* Journal of Environmental Health Science and Engineering, 2014. **12**(1): p. 21.

47. Feng, Q., et al., *Synthesis and characterization of Fe3O4/ZnO-GO nanocomposites with improved photocatalytic degradation methyl orange under visible light irradiation.* Journal of Alloys and Compounds, 2018. **737**: p. 197-206.
48. Długosz, O., et al., *Synthesis of Fe3O4/ZnO nanoparticles and their application for the photodegradation of anionic and cationic dyes.* International Journal of Environmental Science and Technology, 2021. **18**(3): p. 561-574.
49. Li, Y.-Q., S.-Y. Fu, and Y.-W. Mai, *Preparation and characterization of transparent ZnO/epoxy nanocomposites with high-UV shielding efficiency.* Polymer, 2006. **47**(6): p. 2127-2132.
50. Elshypany, R., et al., *Magnetic ZnO Crystal Nanoparticle Growth on Reduced Graphene Oxide for Enhanced Photocatalytic Performance under Visible Light Irradiation.* Molecules, 2021. **26**(8).
51. Huo, R., et al., *Enhanced photocatalytic performances of hierarchical ZnO/ZnAl2O4 microsphere derived from layered double hydroxide precursor spray-dried microsphere.* Journal of colloid and interface science, 2013. **407**: p. 17-21.
52. Farimani, M.H.R., et al., *Study of structural and magnetic properties of superparamagnetic Fe3O4/SiO2 core–shell nanocomposites synthesized with hydrophilic citrate-modified Fe3O4 seeds via a sol–gel approach.* Physica E: Low-dimensional Systems and Nanostructures, 2013. **53**: p. 207-216.
53. Li, G.-Y., et al., *Kinetics of adsorption of Saccharomyces cerevisiae mandelated dehydrogenase on magnetic Fe3O4–chitosan nanoparticles.* Colloids and Surfaces A: Physicochemical and Engineering Aspects, 2008. **320**(1-3): p. 11-18.
54. Arguello, C., D.L. Rousseau, and S.d.S. Porto, *First-order Raman effect in wurtzite-type crystals.* Physical Review, 1969. **181**(3): p. 1351.
55. Cuscó, R., et al., *Temperature dependence of Raman scattering in ZnO.* Physical Review B, 2007. **75**(16): p. 165202.
56. Ashkenov, N., et al., *Infrared dielectric functions and phonon modes of high-quality ZnO films.* Journal of Applied Physics, 2003. **93**(1): p. 126-133.
57. Mukhtar, A., et al., *Structural characterization of self-assembled chain like Fe-FeOx Core shell nanostructure.* Nanoscale Research Letters, 2019. **14**(1): p. 308.
58. Yew, Y.P., et al., *An eco-friendly means of biosynthesis of superparamagnetic magnetite nanoparticles via marine polymer.* IEEE Transactions on Nanotechnology, 2017. **16**(6): p. 1047-1052.
59. Zou, P., et al., *Multifunctional Fe3O4/ZnO nanocomposites with magnetic and optical properties.* Journal of nanoscience and nanotechnology, 2010. **10**(3): p. 1992-1997.
60. Shirzad-Siboni, M., et al., *Photocatalytic reduction of hexavalent chromium over ZnO nanorods immobilized on kaolin.* Industrial & Engineering Chemistry Research, 2014. **53**(3): p. 1079-1087.
61. Sun, H., L. Cao, and L. Lu, *Magnetite/reduced graphene oxide nanocomposites: one step solvothermal synthesis and use as a novel platform for removal of dye pollutants.* Nano Research, 2011. **4**(6): p. 550-562.
62. Wang, L., et al., *Water-soluble Fe_3O_4 nanoparticles with high solubility for removal of heavy-metal ions from waste water.* Dalton Transactions, 2012. **41**(15): p. 4544-4551.
63. Farrokhi, M., et al., *Application of ZnO–Fe_3O_4 nanocomposite on the removal of azo dye from aqueous solutions: kinetics and equilibrium studies.* Water, Air, & Soil Pollution, 2014. **225**(9): p. 2113.

64. Guo, C., et al., *Flowerlike iron oxide nanostructures and their application in microwave absorption.* Journal of Alloys and Compounds, 2015. **631**: p. 183-191.
65. Yu, J., et al., *Duality in the mechanism of hexagonal ZnO/CuxO nanowires inducing sulfamethazine degradation under solar or visible light.* Catalysts, 2019. **9**(11): p. 916.
66. Qu, G., et al., *Graphene-modified ZnO nanostructures for low-temperature NO2 sensing.* ACS omega, 2019. **4**(2): p. 4221-4232.
67. Laurent, S., et al., *Magnetic iron oxide nanoparticles: synthesis, stabilization, vectorization, physicochemical characterizations, and biological applications.* Chemical reviews, 2008. **108**(6): p. 2064-2110.
68. Oprea, O., et al., *THE INFLUENCE OF THE THERMAL TREATMENT ON LUMINESCENCE PROPERTIES OF ZnO.* Digest Journal of Nanomaterials & Biostructures (DJNB), 2013. **8**(2).
69. Bolton, J.R., et al., *Figures-of-merit for the technical development and application of advanced oxidation technologies for both electric-and solar-driven systems (IUPAC Technical Report).* Pure and Applied Chemistry, 2001. **73**(4): p. 627-637.
70. Bolton, J.R., et al., *Figures-of-merit for the technical development and application of advanced oxidation processes.* Journal of advanced oxidation technologies, 1996. **1**(1): p. 13-17.
71. Wang, H., et al., *Synthesis of rectorite/Fe3O4/ZnO composites and their application for the removal of methylene blue dye.* Catalysts, 2018. **8**(3): p. 107.
72. Nada, A.A., et al., *BN/GdxTi$_{(1-x)}$O$_{(4-x)/2}$nanofibers for enhanced photocatalytic hydrogen production under visible light.* Applied Catalysis B: Environmental, 2019. **251**: p. 76-86.
73. Fan, H., et al., *Synthesis of metal-phase-assisted 1T@ 2H-MoS$_2$ nanosheet-coated black TiO$_2$ spheres with visible light photocatalytic activities.* Journal of Materials Science, 2018. **53**(14): p. 10302-10312.
74. Marsooli, M.A., et al., *Preparation and characterization of magnetic Fe3O4/CdWO4 and Fe3O4/CdWO4/PrVO4 nanoparticles and investigation of their photocatalytic and anticancer properties on PANC1 cells.* Materials, 2019. **12**(19): p. 3274.
75. Ismail, A.A., M. Faisal, and A. Al-Haddad, *Mesoporous WO3-graphene photocatalyst for photocatalytic degradation of Methylene Blue dye under visible light illumination.* Journal of Environmental Sciences, 2018. **66**: p. 328-337.
76. Sobahi, T.R., et al., *Photocatalytic degradation of methylene blue dye in water using Pt/ZnO-MWCNT under visible light.* Nanoscience and Nanotechnology Letters, 2017. **9**(2): p. 144-150.
77. Wang, Q., et al., *Zn$_3$(OH)2V$_2$O$_7$· 2H$_2$O/g-C$_3$N$_4$: a novel composite for efficient photodegradation of methylene blue under visible-light irradiation.* Applied Surface Science, 2015. **347**: p. 602-609.
78. Marsooli, M.A., et al., *Synthesis of Magnetic Fe$_3$O$_4$/ZnWO4 and Fe$_3$O$_4$/ZnWO$_4$/CeVO$_4$ Nanoparticles: The Photocatalytic Effects on Organic Pollutants upon Irradiation with UV-Vis Light.* Catalysts, 2020. **10**(5): p. 494.
79. Zhu, B., et al., *Photocatalytic degradation of polyacrylamide by rGO@Fe3O4/Cu2O@ZnO magnetic recyclable composites.* Materials Science in Semiconductor Processing, 2021. **131**: p. 105841.
80. Talukdar, K., et al., *Novel Z-scheme Ag3PO4/Fe3O4-activated biochar photocatalyst with enhanced visible-light catalytic performance toward degradation of bisphenol A.* Journal of Hazardous Materials, 2020. **398**: p. 123025.

81. Abo-Farha, S., *Photocatalytic degradation of monoazo and diazo dyes in wastewater on nanometer-sized TiO2.* Journal of American science, 2010. **6**(11): p. 130-42.
82. Shanthi, M. and V. Kuzhalosai, *Photocatalytic degradation of an azo dye, Acid Red 27, in aqueous solution using nano ZnO.* 2012.